Effects of a nonadiabatic wall on supersonic shock/boundary-layer interactions

Pedro S. Volpiani,[1] Matteo Bernardini,[2] and Johan Larsson[1]
[1]*Department of Mechanical Engineering, University of Maryland, College Park, Maryland 20742, USA*
[2]*Dipartimento di Ingegneria Meccanica e Aerospaziale, Università di Roma "La Sapienza," Via Eudossiana 18, 00184 Rome, Italy*

(Received 30 April 2018; published 22 August 2018)

Direct numerical simulations are employed to investigate a shock wave impinging on a turbulent boundary layer at free-stream Mach number $M_\infty = 2.28$ with different wall thermal conditions, including adiabatic, cooled, and heated, for a wide range of deflection angles. It is found that the thermal boundary condition at the wall has a large effect on the size of the interaction region and on the level of pressure fluctuations. The distribution of the Stanton number shows a good agreement with prior experimental studies and confirms the strong heat transfer and complex pattern within the interaction region. An effort was also made to describe the unsteady features of the flow by means of wall pressure and heat flux spectra. Numerical results indicate that the changes in the interaction length due to the wall thermal condition are mainly linked to the incoming boundary layer, which is in agreement with previous experimental studies.

DOI: 10.1103/PhysRevFluids.3.083401

I. INTRODUCTION

Shock/boundary-layer interactions (SBLI) appear in many external and internal flow problems in the aeronautical and aerospace industry, most commonly with a negative impact on the performance of the aircraft. They can increase the aerodynamic drag and modify the heat exchange near the wall considerably. Moreover, if the interaction is strong, low-frequency unsteadiness associated with the separation bubble may occur with resulting strong pressure load variations, yielding structural failure and compromising the maneuverability of the aircraft.

The majority of the research dealing with supersonic shock/boundary-layer interactions considers two canonical geometries: the compression ramp and the flat plate with an impinging shock [1–5]. Many experimental [6–12] and numerical [13–23] studies have contributed to a better understanding of the general topology of this type of flow. Many experimental studies have featured nonadiabatic walls, particularly those in short-duration, high-enthalpy facilities; however, only a few experiments have systematically studied the effect of the wall thermal condition on the SBLI flow field [24–29]. On the numerical side, the number of works that investigated the effect of the wall thermal condition for turbulent SBLI is even more scarce [30].

Spaid and Frishett [24] investigated the effect of heat transfer in SBLI over a compression ramp at free-stream Mach number $M_\infty = 2.9$ for two types of wall conditions: a cold wall (wall-to-recovery-temperature ratio $T_w/T_r = 0.47$) and quasiadiabatic wall ($T_w/T_r = 1.05$). Back and Cuffel [25] analyzed an oblique shock wave impinging on a turbulent boundary layer at $M_\infty = 3.5$ and surface cooling of $T_w/T_r = 0.44$. Both studies found that the effect of wall cooling was to increase the incipient separation angle and reduce the separation distance.

Hayashi *et al.* [26] carried out detailed measurements of the heat transfer in the interaction of incident shock waves and a $M_\infty = 4$ boundary layer developing over an isothermal cold wall ($T_w/T_r \approx 0.6$). They reported a complex behavior of the heat transfer coefficient in the interaction

region, characterized by a sharp increase at the point where the pressure begins to increase, a reduction within the separation bubble, followed by a further increase in the proximity of the reattachment point.

Nonintrusive techniques were used by Schülein [27] to measure the skin-friction coefficient and the heat transfer rate in a SBLI of an impinging shock at $M_\infty = 5$. They found a strong increase of the heat flux in the separation zone, characterized by a complex nonequilibrium behavior.

Surface heat transfer was also assessed by Sandham *et al.* [28] in a transitional SBLI at $M_\infty = 6$, allowing the peak Stanton number in the reattachment regime to be mapped over a range of intermittency states of the approaching boundary layer. They showed that the highest levels of wall heat transfer were consistently obtained for transitional rather than fully turbulent interactions.

More recently, Jaunet *et al.* [29] investigated experimentally the impact of changing the wall temperature on a $M_\infty = 2.3$ shock-induced boundary-layer separation. They varied the shock deflection angle from 3.5° to 9.5° and the wall-to-recovery-temperature ratio from $T_w/T_r = 1$ (adiabatic) to $T_w/T_r = 1.9$ (heated condition). They used Schlieren visualizations, particle image velocimetry (PIV), and time-resolved hot-wire measurements to describe how the wall temperature influences the interaction. Their study resulted in three mean observations about the effects of increasing the wall temperature: (i) a significant increase in the interaction length; (ii) a shift to smaller flow deflections of the onset of separation; and (iii) increased low-frequency activity of the separated flow. They proposed a scaling relationship that was found to accurately describe the changes in the interaction length.

Only recently, the influence of the wall temperature on the behavior of oblique shock waves turbulent boundary layer interactions was investigated using numerical simulations. Bernardini *et al.* [30] carried out direct numerical simulations (DNS, with a numerically captured shock wave) of SBLI at $M_\infty = 2.28$ and a flow deflection of $\phi = 8°$ for five values of the wall-to-recovery-temperature ratio (T_w/T_r): 0.5, 0.75, 1.0 (adiabatic), 1.4, and 1.9. One of the conclusions of this work was that wall cooling could be considered for flow control since it reduces considerably the interaction scales and sizes of the separation bubble. The opposite holds for wall heating. Nevertheless, this study also showed that the maximum thermal and dynamic loads are found for the case of cold wall.

In this paper, we replicate the experiment by Jaunet *et al.* [29] using DNS at a reduced Reynolds number in order to save computational cost. While the experiments were performed at a Reynolds number based on the momentum thickness of $\mathrm{Re}_\theta \approx 5 \times 10^3$, most of our DNS were performed at $\mathrm{Re}_\theta \approx 1 \times 10^3$. We compute the flow at the two wall temperatures in the experiment (T_w/T_r of 1.0 and 1.9) and also at an additional cooled case with $T_w/T_r = 0.5$. This study extends the previous work by Bernardini *et al.* [30] and presents a much larger DNS database, with the main aim of discussing not only the effect of wall temperature but also the effect of the shock strength on the SBLI flow field. The SBLI length scales are discussed and compared with experimental data. The low-frequency unsteadiness is investigated for a subset of the cases which are run for longer times.

II. NUMERICAL APPROACH

The three-dimensional compressible Navier-Stokes equations for an ideal gas are solved in conservative form in a Cartesian coordinate frame:

$$\partial_t \mathbf{Q} + \partial_j \mathbf{F}_i - \partial_j \mathbf{F}_v = 0.$$

The state vector $\mathbf{Q} = [\rho, \rho u_i, \rho E]^T$ consists of density ρ, momentum ρu_i, and total energy $\rho E = p/(\gamma - 1) + \rho u_i^2/2$, where p is the pressure and u_i is the velocity component in direction i. The ratio of specific heats is constant $\gamma = 1.4$. The inviscid and viscous fluxes are, respectively,

$$\mathbf{F}_i = [\rho u_j, \rho u_i u_j + p\delta_{ij}, (\rho E + p)u_j], \quad \mathbf{F}_v = [0, \tau_{ij}, u_i \tau_{ij} + q_j].$$

The fluid is assumed to be Newtonian, and according to the Stokes hypothesis, the viscous stress tensor is given by

$$\tau_{ij} = \mu\left(\frac{\partial u_i}{\partial x_j} + \frac{\partial u_j}{\partial x_i} - \frac{2}{3}\frac{\partial u_k}{\partial x_k}\delta_{ij}\right).$$

The heat flux is modeled by Fourier's law as

$$q_j = -\frac{C_p\mu}{Pr}\partial_j T.$$

The viscosity is assumed to follow the power law $\mu = \mu_{\rm ref}(T/T_{\rm ref})^{3/4}$, and the Prandtl number is taken as $\Pr = 0.7$.

The system of equations are nondimensionalized by the free-stream values of velocity, temperature, and density and the boundary layer thickness. The fluid is assumed to behave as an ideal gas with equation of state $p = R\rho T$, where the nondimensional gas constant is $R = 1/(\gamma M_\infty^2)$. The specific heat is $C_p = \gamma R/(\gamma - 1)$.

The governing equations are solved using an in-house finite-difference code based on a hybrid numerical scheme. Near shocks, a fifth-order-accurate weighted essentially nonoscillatory (WENO) scheme with Roe flux splitting is used to approximate the inviscid fluxes, whereas a sixth-order-accurate central difference scheme in the split form by Ducros *et al.* [31] is used in the remainder of the domain. The sensor $s = -\xi/(|\xi| + \langle\omega_j\omega_j\rangle^{1/2})$ is used to identify regions of shock waves at every time step, where $\xi = \partial_j u_j$ is the dilatation, $\omega_i = \epsilon_{ijk}\partial_j u_k$ is the vorticity, and $\langle\cdot\rangle$ is a local average. The WENO scheme is applied in regions where $s > 0.7$. The viscous terms are treated by a conservative scheme that has the resolution characteristics of a sixth-order scheme, and the system is integrated in time using a fourth-order-accurate Runge-Kutta method. The code has been thoroughly verified on several benchmark problems [32].

The computational domain for all cases has an overall extent $L_x \times L_y \times L_z = 65\delta_{\rm in} \times 18\delta_{\rm in} \times 5\delta_{\rm in}$, where $\delta_{\rm in}$ is the boundary layer thickness at the inlet. Grid nodes are uniformly distributed in the spanwise (z) and streamwise (x) directions. For the wall-normal direction (y), a stretching function based on a hyperbolic cosine mapping is used, in order to gather points closer to the wall.

Periodicity is imposed in the spanwise direction. The oblique shock is generated at the top boundary by imposing the inviscid oblique shock solution corresponding to each flow deflection angle. The inflow turbulence is generated using the digital filtering technique by Klein *et al.* [33] and Touber and Sandham [17]. Digital filtering avoids the introduction of any spurious low frequencies (that are unavoidable in recycling-type methods, though they can be made very small). In this study, filtering length scales of 0.6 and 0.2 $\delta_{\rm in}$ are used in the streamwise and spanwise directions. The length scale in the wall-normal direction is taken as 0.04 $\delta_{\rm in}$ near the wall and 0.2 $\delta_{\rm in}$ in the free stream, with a smooth transition in between. The mean velocity and Reynolds stress profiles are taken from auxiliary boundary layer simulations at each T_w/T_r and Reynolds number, in order to ensure realistic profiles at each wall temperature condition. The mean temperature and density are assumed to follow Walz's relation [Eq. (4), to be discussed below], and the fluctuating quantities are assumed to follow the strong Reynolds analogy (cf. Ref. [2]).

III. SUPERSONIC BOUNDARY LAYER SIMULATIONS

We first consider simulations without the impinging shock to assess and validate the inflow condition and the state of the turbulent boundary layer. Three wall-to-recovery-temperature ratios T_w/T_r are considered in this study: 1.0 (adiabatic), 1.9 (heated), and 0.5 (cooled). The recovery temperature T_r is computed as (cf. Ref. [2])

$$\frac{T_r}{T_\infty} = 1 + r\frac{\gamma - 1}{2}M_\infty^2, \tag{1}$$

TABLE I. Mesh configuration for the DNS of supersonic boundary layers. The table presents the wall-to-recovery-temperature ratio T_w/T_r, the number of points, and the grid spacing in terms of wall units in each directions.

Simulation	T_w/T_r	N_x	N_y	N_z	Δx^+	Δy_w^+	Δz^+
BL-1.0	1.0	1536	384	128	6.0	0.6	5.6
BL-1.9	1.9	1536	320	128	2.4	0.6	2.4
BL-0.5	0.5	1800	480	256	11	0.6	6.4
BL-1.0-hRe	1.0	1800	480	256	9.6	0.8	5.3

where the subscript ∞ denotes conditions at the edge of the boundary layer, that is, in the local free stream, so that the edge Mach number $M_\infty = U_\infty/\sqrt{\gamma R T_\infty}$. The recovery factor is taken as $r = \mathrm{Pr}^{1/3}$.

Details of the mesh are given in Table I. Note that wall cooling leads to a drastic reduction in the viscous length scale, which leads to much more demanding grid requirements for the cold wall case. Note also that the strictest grid requirements for the heated case come from the outer part of the boundary layer, leading to this case having an excessively fine grid spacing in viscous units near the wall.

There are many Reynolds numbers for compressible boundary layers, and they all scale differently with Mach number and the wall thermal boundary condition. In this study, we want to vary the T_w/T_r ratio while keeping other factors fixed. So, a valuable question is which Reynolds number we should keep fixed in order to keep the turbulence similar between cases. The traditional choice ever since Fernholz and Finley [34] has been $\mathrm{Re}_{\delta_2} = \rho_\infty u_\infty \theta/\mu_w$, where θ is the momentum thickness. More recent work on the scaling of the mean velocity profile under nonadiabatic conditions [35] suggests that the Reynolds number Re_τ^* (the friction Re of the transformed, supposedly universal, state) should be held constant. However, the latter study only analyzed compressible channel flows in detail, and hence the question of which Reynolds number is the most relevant for boundary layers is a partially open question. For SBLI flows, there is no data on whether Re_τ^* is a meaningful Reynolds number. Given all this, the decision in this study was to compute all three T_w/T_r cases at fixed $\mathrm{Re}_\tau^* \approx 500$, and then to consider an additional case BL-1.0-hRe which matches the Re_{δ_2} of the cooled case.

Figure 1(a) shows the Van Driest–transformed mean velocity profile for the simulation with an adiabatic wall at the location $x_0 = 35\delta_{\mathrm{in}}$, which will later be the inviscid impingement point for the shock. The Reynolds numbers at this station are listed in Table II. The density-scaled Reynolds

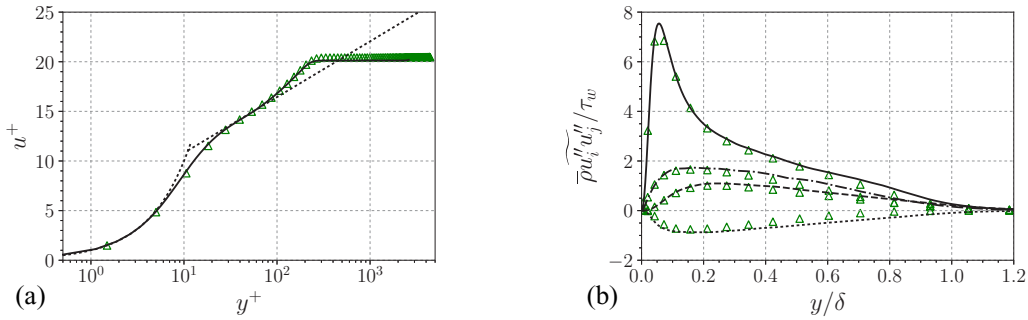

FIG. 1. Comparison of the adiabatic ($T_w/T_r = 1$) boundary layer at station $x_0 = 35\delta_{\mathrm{in}}$ (lines) with the incompressible DNS results of Schlatter and Örlü [36] at $\mathrm{Re}_\theta = 670$ (triangles). (a) Van Driest–transformed mean velocity profile (solid line). The linear $u^+ = y^+$ and log-law $u^+ = 5.2 + 2.44 \ln y^+$ are also represented (dotted lines). (b) Density-scaled Reynolds stress components: longitudinal (solid), wall-normal (dashed), transverse (dot-dashed), and shear stress (dotted line).

TABLE II. Global characteristics of the turbulent boundary layers at $x_0 = 35\delta_{\text{in}}$. The Reynolds numbers are defined as $\text{Re}_\delta = \rho_\infty u_\infty \delta_0/\mu_\infty$, $\text{Re}_\theta = \rho_\infty u_\infty \theta/\mu_\infty$, $\text{Re}_{\delta_2} = \rho_\infty u_\infty \theta/\mu_w$, $\text{Re}_\tau = \rho_w u_\tau \delta/\mu_w$, and $\text{Re}^*_\tau = \rho_\infty(\tau_w/\rho_\infty)^{1/2}\delta/\mu_\infty$, where θ is the momentum thickness and u_τ is the friction velocity.

Simulation	Re_δ	Re_θ	Re_{δ_2}	Re_τ	Re^*_τ
BL-1.0	12 628	1047	642	224	500
BL-1.9	13 440	868	328	100	498
BL-0.5	12 000	1250	1287	511	488
BL-1.0-hRe	24 327	1990	1220	395	885

stresses are shown in Fig. 1(b). The incompressible DNS results of Schlatter and Örlü [36] at a similar Reynolds number ($\text{Re}_\theta = \text{Re}_{\delta_2} = 670$ and $\text{Re}_\tau = 250$) is also shown in Fig. 1 and compare well with the present mean velocity and rms profiles. This provides confidence that the present inflow boundary condition and the development length of $35\delta_{\text{in}}$ are sufficient to produce realistic turbulence. For reference, $\delta_0/\delta_{\text{in}} \approx 1.6$ with slight variations among the different cases.

Figure 2(a) shows the mean velocity profiles from all three wall temperatures. The profiles are transformed using the Van Driest transformation

$$u^+ = \int_0^{u^+} \left(\frac{\overline{\rho}}{\rho_w}\right)^{1/2} du^+, \tag{2}$$

which is meant to be used with the standard y^+ scaled wall-normal coordinate ($y^+ = y\sqrt{\rho_w \tau_w}/\mu_w$). The profiles are also shown after applying the more recent transformation by Trettel and Larsson [35], where

$$y^+_{TL} = \frac{y\overline{\rho}}{\overline{\mu}}\sqrt{\frac{\tau_w}{\overline{\rho}}}, \tag{3a}$$

$$u^+_{TL} = \int_0^{u^+} \left(\frac{\overline{\rho}}{\rho_w}\right)^{1/2}\left[1 + \frac{1}{2}\frac{1}{\overline{\rho}}\frac{d\overline{\rho}}{dy}y - \frac{1}{\overline{\mu}}\frac{d\overline{\mu}}{dy}y\right]du^+ = \int_0^{u^+}\left(\frac{\overline{\mu}}{\mu_w}\right)\frac{dy^+_{TL}}{dy^+}du^+. \tag{3b}$$

Note that this transformation affects both the velocity and the wall-normal coordinate; i.e., u^+_{TL} must be plotted vs y^+_{TL}. This "coupling" between the velocity and the coordinate is explicit in the second form of the velocity transformation (3b). Also note that y^+_{TL} is more commonly referred to

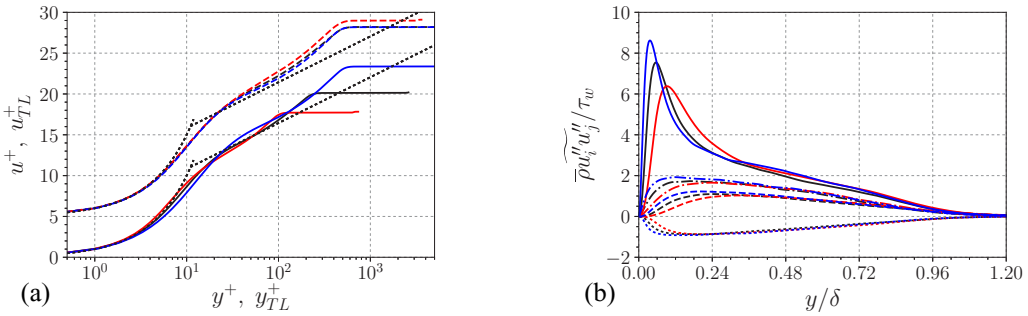

FIG. 2. Assessment of the boundary layer at station $x_0 = 35\delta_{\text{in}}$. (a) Van Driest–transformed mean velocity u^+ plotted vs $y^+ = y\sqrt{\rho_w\tau_w}/\mu_w$ (solid lines), compared to the velocity transformed according to Ref. [35], u^+_{TL} plotted vs the semilocally scaled y^+_{TL} (dashed lines, shifted vertically). (b) Density-scaled Reynolds stress components: longitudinal (solid), wall-normal (dashed), transverse (dot-dashed), and shear stress (dotted line). Black lines refer to the adiabatic case BL-1.0, red lines refer to the heated case BL-1.9, and blue lines refer to the cooled case BL-0.5.

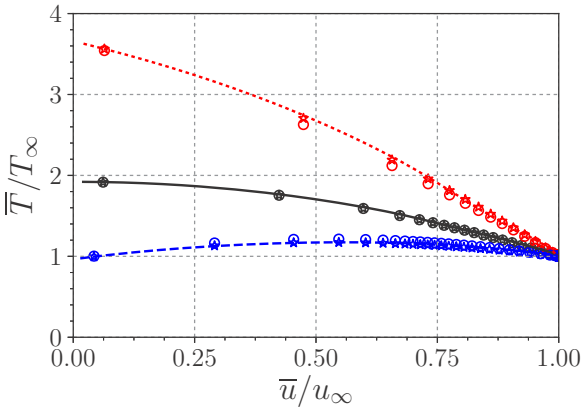

FIG. 3. The temperature-velocity relationship at station $x_0 = 35\delta_{\text{in}}$ for BL-1.0 (solid), BL-1.9 (dotted), and BL-0.5 (dashed line). The circles (○) indicate the Walz solution and the stars (☆) denote the solution given by Zhang *et al.* [39].

as the semilocal scaling y^*; we use the present notation here to avoid confusion with the interaction coordinates x^* and y^* to be introduced below.

The results in Fig. 2(a) show a much better collapse in the buffer layer with the transformation in Eq. (3). The profiles do not collapse perfectly in the log layer, either with each other or with the log law, which stands in contrast to the results on channel flows in Ref. [35].

The density-scaled Reynolds stresses are shown for the three simulations in Fig. 2(b). The profiles collapse in the outer part of the boundary layer, but the peak in the inner layer is higher for the cooled case. The reason is probably linked to the relatively low Reynolds numbers here, since prior work [35,37] suggests that the Reynolds stresses should collapse when the transformed Reynolds number Re_τ^* is fixed (as done here). Having said that, both of those prior studies considered channel flows, so it is possible that the lack of collapse of the peak stress points to some difference between boundary layers and channels (with respect to transformations to a supposedly universal state).

It is worth noting that Bernardini *et al.* [30] used a recycling/rescaling inflow boundary condition over an adiabatic wall and then changed the wall temperature at a distance of $54\delta_{\text{in}}$ from the inlet. The shock impingement point was then placed an additional distance of $15.5\delta_{\text{in}}$ from that point. This distance was found to be almost long enough for the mean temperature profile to reach a new equilibrium state but not quite. As discussed above, the present study uses the digital filtering technique at the inflow. More important, we impose the wall temperature throughout the domain and take the inflow profiles from auxiliary simulations at the same wall temperature, which implies that the mean and Reynolds stress profiles at the inlet are near "equilibrium" with respect to the thermal wall condition. This can be seen in Fig. 3, which shows the temperature-velocity relationship. The present DNS agrees relatively well with the classic Walz solution [38] and even better with the generalized Reynolds analogy recently proposed by Zhang *et al.* [39]. These temperature-velocity relations can be written as

$$\frac{\overline{T}}{T_\infty} = \frac{T_w}{T_\infty} + \frac{T_r - T_w}{T_\infty}\frac{\overline{u}}{u_\infty} f\left(\frac{\overline{u}}{u_\infty}\right) + \frac{T_\infty - T_r}{T_\infty}\left(\frac{\overline{u}}{u_\infty}\right)^2, \tag{4}$$

where $f(\overline{u}/u_\infty) = 1$ for the Walz solution and

$$f\left(\frac{\overline{u}}{u_\infty}\right) = \left[1 - \frac{\overline{q}_w u_\infty}{\tau_w C_p (T_w - T_r)}\right]\text{Pr}\left(\frac{\overline{u}}{u_\infty}\right)^2 + \left[\frac{\overline{q}_w u_\infty}{\tau_w C_p (T_w - T_r)}\right]\text{Pr}\left(\frac{\overline{u}}{u_\infty}\right) \tag{5}$$

for the relation developed by Zhang *et al.* [39]. Note that both are identical for the adiabatic case.

TABLE III. Flow parameters for the SBLI simulations at free-stream Mach number $M_\infty = 2.28$. T_w/T_r is the wall-to-recovery-temperature ratio, φ is the incidence angle of the shock generator, L_{sep} is the length of the recirculation bubble, and T is the overall simulation time.

Simulation	T_w/T_r	$\varphi(^\circ)$	T_w/T_∞	Grid points	$Tu_\infty/\delta_{\text{in}}$	Spectra	CPUh
SBLI-1.0-11.0	1.0	11.0°	1.92	76 M	1100	No	40k
SBLI-1.0-9.5	1.0	9.5°	1.92	76 M	2100	Yes	80k
SBLI-1.0-8.0	1.0	8.0°	1.92	76 M	1100	No	40k
SBLI-1.0-6.5	1.0	6.5°	1.92	76 M	1100	No	40k
SBLI-1.0-5.0	1.0	5.0°	1.92	76 M	1100	No	40k
SBLI-1.9-9.5	1.9	9.5°	3.66	63 M	2100	Yes	80k
SBLI-1.9-8.0	1.9	8.0°	3.66	63 M	1100	No	40k
SBLI-1.9-6.5	1.9	6.5°	3.66	63 M	1100	No	40k
SBLI-1.9-5.0	1.9	5.0°	3.66	63 M	1100	No	40k
SBLI-1.9-3.5	1.9	5.0°	3.66	63 M	1100	No	40k
SBLI-0.5-9.5	0.5	9.5°	0.96	221 M	2100	Yes	400k
SBLI-0.5-8.0	0.5	8.0°	0.96	221 M	1100	No	200k
SBLI-adia2heat-9.5	1.0/1.9	9.5°	1.92/3.66	76 M	1100	No	40k
SBLI-heat2adia-9.5	1.9/1.0	9.5°	3.66/1.92	76 M	1100	No	40k
SBLI-1.0-9.5-fine	1.0	9.5°	1.92	171 M	800	No	100k
SBLI-1.0-9.5-hRe	1.0	9.5°	1.92	220 M	1100	No	250k

IV. SBLI SIMULATIONS

In this section, the effect of the flow deflection angle and the wall temperature on the SBLI flow field is analyzed. Discussions about the pressure spectra and the length scale of the interaction are also presented.

The same grid used to run the previous boundary layer cases are employed in the SBLI simulations. The shock impingement point is set at $x_{\text{imp}} = x_0 = 35\delta_{\text{in}}$ for all cases. In the following, the origin is placed at x_{imp} and lengths are made nondimensional with respect to the boundary layer thickness δ_0 at the nondisturbed reference station $x_{\text{imp}} = x_0 = 35\delta_{\text{in}}$. Thus, the nondimensional interaction coordinates are written as $x^* = (x - x_{\text{imp}})/\delta_0$ and $y^* = y/\delta_0$. All SBLI simulations are summarized in Table III.

A. Mesh convergence

A grid refinement study is done by increasing the number of grid points in all directions for the interaction characterized by adiabatic walls and $\varphi = 9.5^\circ$. The standard mesh contains $1536 \times 384 \times 128$ points, while the refined one contains $2048 \times 490 \times 170$ points. The skin friction coefficient is used to identify a grid-independent solution. This quantity is shown in Fig. 4 for both simulations and the agreement is excellent. Note that the simulation using the finer mesh is run for a shorter time to save computational cost. Still, the difference between the separation length is less than 1%. With respect to the cooled case, Trettel and Larsson [35] found grid-converged results for a similar grid resolution but a more strongly cooled case using the same code.

The spanwise domain size is about $3\delta_0$ for all cases, while the size of the separation bubble varies up to $8\delta_0$ in this study. Pasquariello *et al.* [23] performed a careful assessment of the influence of the domain width on the results for a strong SBLI with a separation bubble of size $15\delta_0$ and found virtually unchanged results for domain width down to $2.25\delta_0$. For this reason, the present domain width is believed to be sufficient.

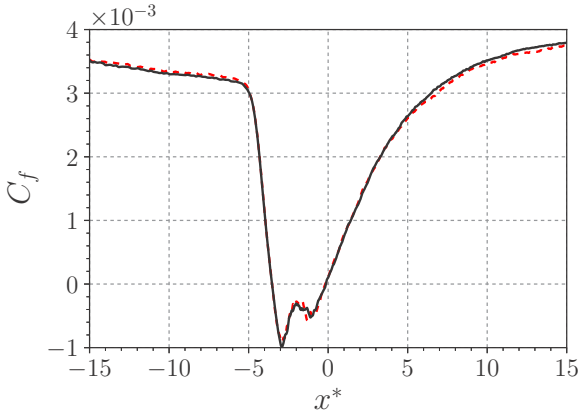

FIG. 4. Grid convergence test. Mean skin friction coefficient for cases SBLI-1.0-9.5 ($1536 \times 384 \times 128$ grid points, solid) and SBLI-1.0-9.5-fine ($2048 \times 490 \times 170$ grid points, dashed line).

B. Instantaneous flow fields

If the strength of the shock is sufficiently large, the boundary layer detaches and the mean pressure profile through the interaction region exhibits a plateau in the separation zone. At the leading edge of the separation bubble, compression waves form the reflected shock. Mixing is enhanced at the shear layer across the interacting shock. The flow deflection at the top of the bubble generates an expansion fan followed by compression waves. Further downstream, the boundary layer recovers an equilibrium state after passing by a relaxation process. The shock motion can exhibit a large-scale streamwise oscillation with a frequency that is two to three orders of magnitude lower than the characteristic frequency of the turbulence in the incoming boundary layer.

To provide an overview of the typical topology of shock-wave turbulent boundary layer interactions, we report in Fig. 5 snapshots of density and its wall-normal derivative (numerical schlieren). These visualizations highlight the turbulent structures of the boundary layer and the complex waves that are originated by the interaction. A three-dimensional snapshot of the SBLI is shown in Fig. 6. The incident and reflecting shocks are identified by plotting an isosurface of

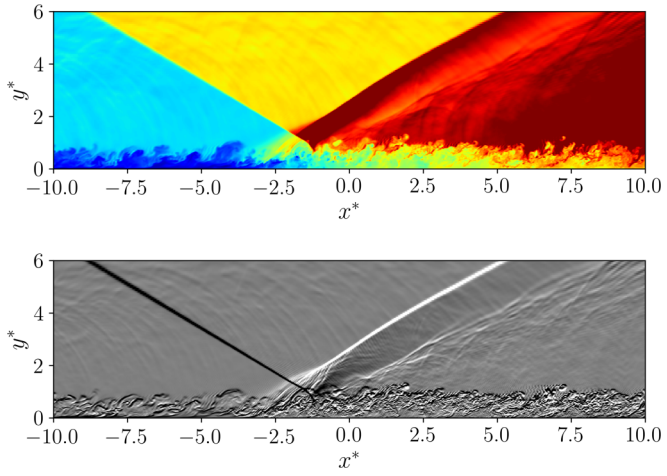

FIG. 5. Contours of the instantaneous density ρ (top) and wall-normal density gradient ρ_y (bottom) fields for the simulation with adiabatic wall condition and $\varphi = 9.5^\circ$ SBLI-1.0-9.5.

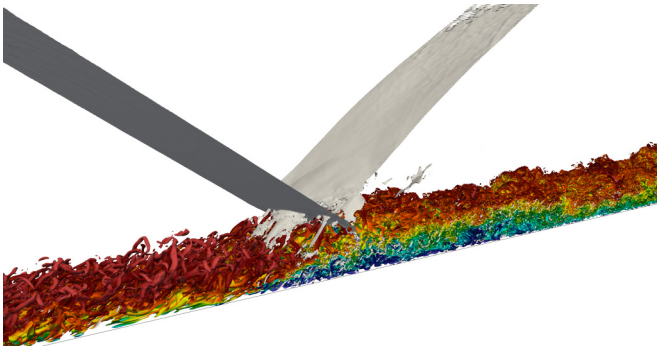

FIG. 6. Isosurface of the Q criterion colored by the streamwise velocity and dilatation isosurface (gray) for the simulation with adiabatic wall condition and $\varphi = 9.5^\circ$ SBLI-1.0-9.5.

dilatation. The turbulence activity is clearly modified after the reflecting shock foot and along the shear layer, in agreement with other numerical studies [18,20].

C. Effect of deflection angle on the SBLI flow field

In this section, simulations with heated wall condition and different deflection angles are analyzed. As expected, the size of the recirculating bubble increases when φ increases. This behavior is confirmed when analyzing the average skin friction coefficient $C_f = 2\tau_w/\rho_\infty u_\infty^2$, shown in Fig. 7(a).

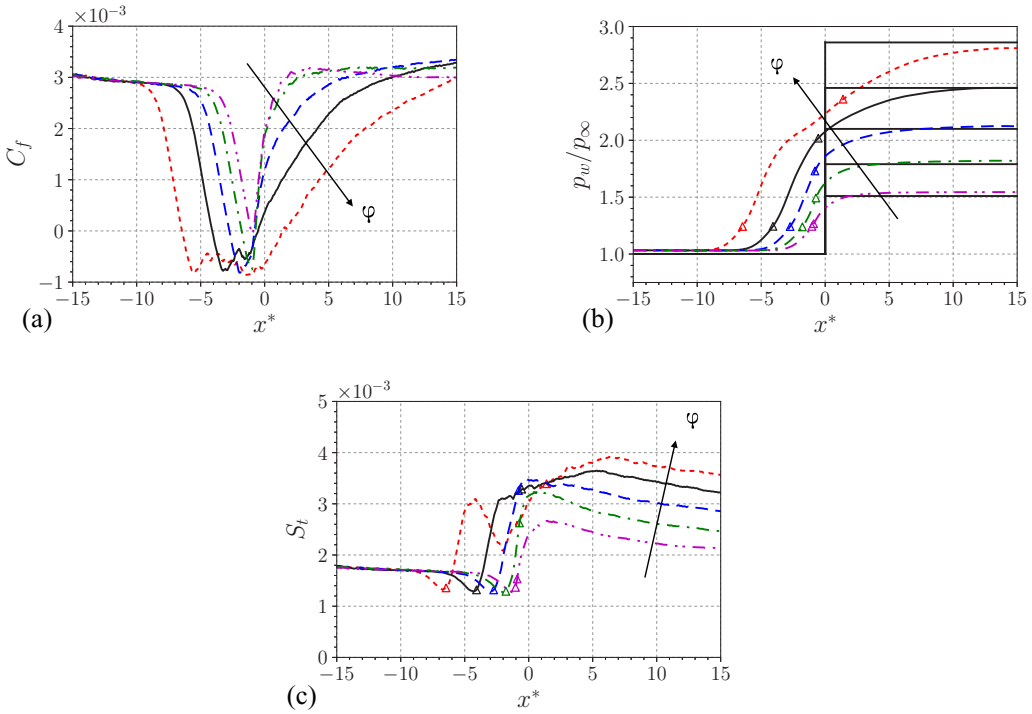

FIG. 7. Distribution of the (a) mean skin friction coefficient, (b) mean wall pressure, and (c) Stanton number across the interaction zone at various incidence angle of the shock generator: $\varphi = 9.5^\circ$ (case SBLI-1.9-9.5, dotted), $\varphi = 8.0^\circ$ (case SBLI-1.9-8.0, solid), $\varphi = 6.5^\circ$ (case SBLI-1.9-6.5, dashed), $\varphi = 5.0^\circ$ (case SBLI-1.9-5.0, dash-dotted), and $\varphi = 3.5^\circ$ (case SBLI-1.9-6.5, dash-double-dotted line). Triangles indicate separation and reattachment position.

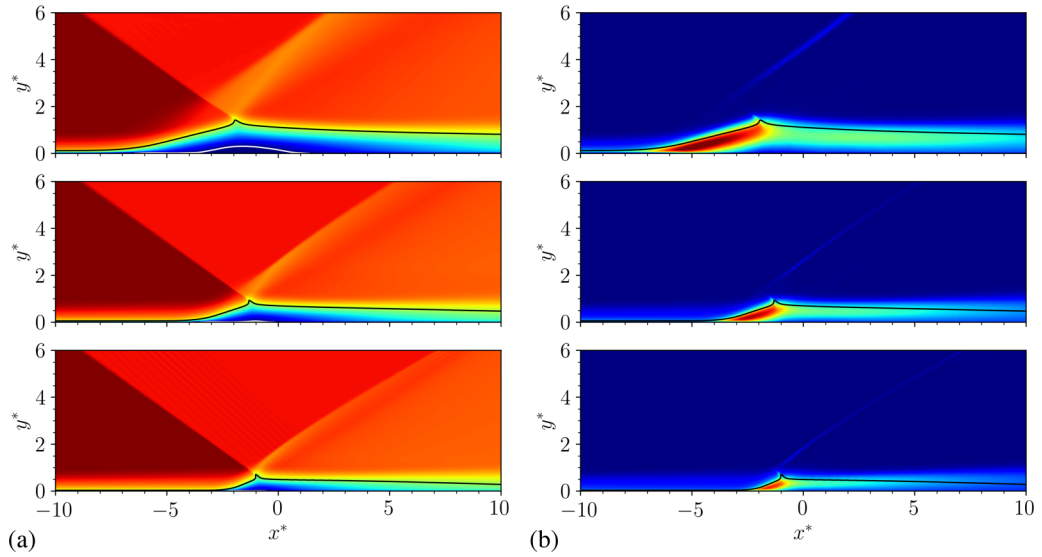

FIG. 8. Mean streamwise velocity field $\overline{u}$ (left) and mean turbulence kinetic energy $k = \widetilde{u_i'' u_i''}/2$ (right) at various wall-to-recovery-temperature ratios: cases SBLI-1.9-9.5, SBLI-1.0-9.5, and SBLI-0.5-9.5 from top to bottom. Contour levels are shown in the range $0 < \overline{u}/u_\infty < 1$ and $0 < k/u_\infty^2 < 0.04$. The black line denotes the sonic line and the white line denotes the zero level.

The mean separation location [also labeled in Fig. 7(b)] is highly dependent on the flow condition and moves upstream for higher deflection angles. The reattachment point is much less affected by the change in the deflection angle and remains practically constant for the majority of the simulated cases. Only for the strong interaction (case SBLI-1.9-9.5) does the reattachment point move downstream. The mean wall pressure normalized by the free-stream pressure is displayed in Fig. 7(b). For all presented cases, the pressure jump predicted by the inviscid theory is well recovered by the direct numerical simulations.

The effect of heating or cooling on the heat transfer rate can be characterized by the spatial distribution of the Stanton number, which is defined as

$$\mathrm{St} = \frac{q_w}{\rho_\infty u_\infty C_p (T_w - T_r)}, \qquad q_w = -k \left. \frac{d\overline{T}}{dy} \right|_w . \tag{6}$$

This quantity is plotted in Fig. 7(c). Note that a similar normalization has been employed by Hayashi *et al.* [26], who measured the heat transfer coefficient in experiments with a cooled wall. The complex pattern observed experimentally is confirmed in the present study. The Stanton distribution reaches its minimum value close to the separation point (Hayashi *et al.* associated this point with where the pressure started to increase) and then it sharply increases within the interaction zone. If the interaction is strong enough (high deflection angle in Hayashi *et al.* or case SBLI-1.9-9.5 presented herein), after reaching a local maximum, the Stanton number exhibits a curvature change with a second minimum around the reattachment point and then increases again, attaining a second broad maximum in the downstream relaxation region. Note that the Stanton distribution for cases with $\varphi < 8^\circ$ are typical of weak interactions.

D. Effect of wall temperature on the SBLI flow field

The mean streamwise velocity fields in the xy plane are reported in Fig. 8(a) for different wall-to-recovery-temperature ratio and same deflection angle $\varphi = 9.5^\circ$. The influence of the wall temperature

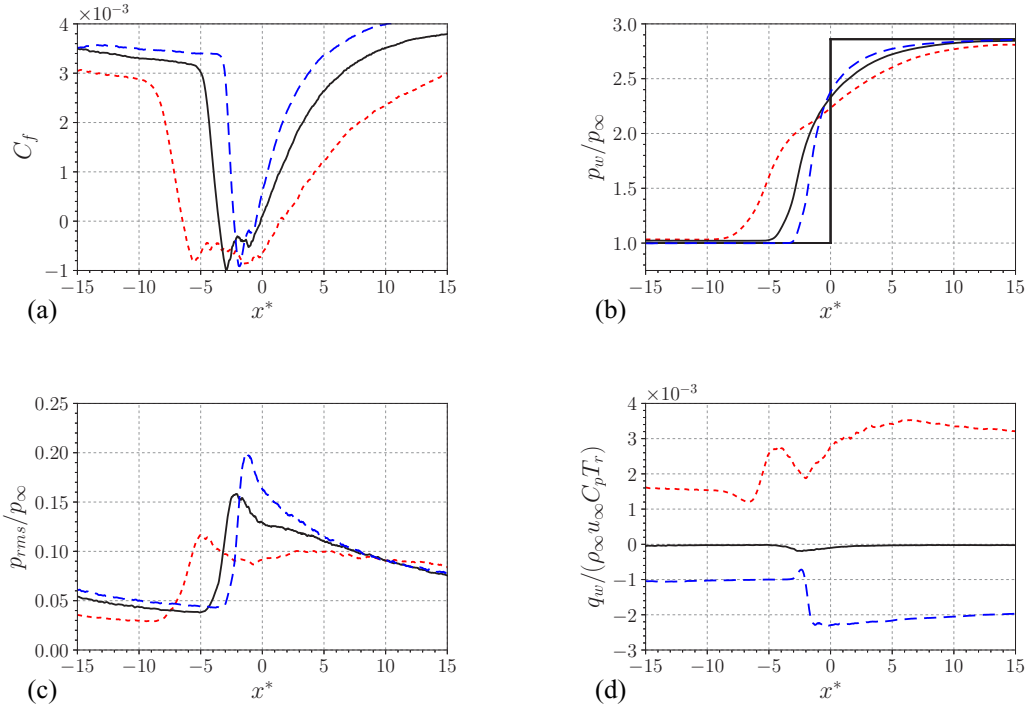

FIG. 9. Distribution of the (a) mean skin friction coefficient, (b) mean wall pressure, (c) root-mean-square wall pressure, and (d) mean wall heat flux across the interaction zone at various wall-to-recovery-temperature ratios and deflection angle 9.5°. Cases SBLI-1.9-9.5 (dotted), SBLI-1.0-9.5 (solid), and SBLI-0.5-9.5 (dashed lines).

on the size of the recirculation bubble is evident, with higher wall temperature inducing a larger recirculation zone. When the wall temperature is increased, the density is lowered close to the wall, decreasing the average momentum flux in the boundary layer. As a result, separation is more likely to occur. The interaction length scale, L_{int}, defined as the distance between the nominal incoming shock impingement point (x_{imp}) and the apparent origin of the reflected shock (x_{ref}), is also affected by the wall-to-recovery-temperature ratio. As already mentioned by Bernardini *et al.* [30], the interaction length scale increases (decreases) with wall heating (cooling).

In order to measure qualitatively the turbulence activity within the interaction, the turbulence kinetic energy $k = \widetilde{u_i'' u_i''}/2$ is displayed in Fig. 8(b). Compared to the adiabatic case, the turbulence kinetic energy k increases (decreases) when wall heating (cooling) is employed. We emphasize the fact that the turbulence activity is primarily present in the first part of the interaction zone. This behavior is associated with the development of a shear layer at the separation shock and is consistent with other numerical [30] and experimental [9] studies.

The spatial distribution of the mean skin friction coefficient C_f, shown in Fig. 9(a), proves the existence of a separation bubble. After the friction coefficient plateau, a slow recovery toward boundary layer equilibrium is observed. If compared to the adiabatic case SBLI-1.0-9.5, the size of the separation length L_{sep} in simulation SBLI-1.9-9.5 is increased by a factor of ≈2.3. On the other hand, a reduction of a factor ≈2 is observed in simulation with cooled walls SBLI-0.5-9.5.

The spatial distribution of the mean wall pressure p_w for the same cases, as well as the pressure jump predicted by the inviscid theory are plotted in Fig. 9(b). Heating the wall induces a shift upstream of the beginning of the interaction, engendering a smoother pressure rise. The reverse behavior is observed when cooling is present: the beginning of the interaction is shifted downstream, leading

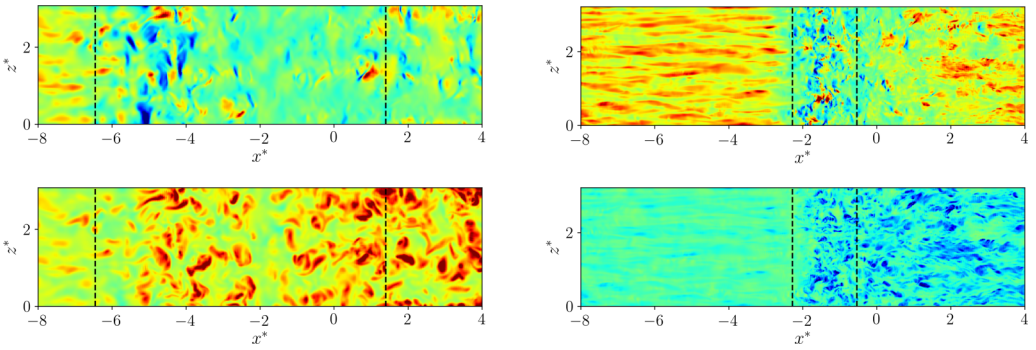

FIG. 10. Instantaneous contours of skin friction (top) and normalized heat flux (bottom) for heated SBLI-1.9-9.5 (left) and cooled SBLI-0.5-9.5 (right) cases. Dashed lines indicate the mean separation and reattachment positions.

to a steeper variation of p_w within the interaction zone. The same pattern is noticed when vortex generators are used in order to control separation [40]. In the heated case, it is possible to note two bumps in the pressure signal, which are a characteristic of strong interactions. As explained in Ref. [3], the first pressure rise occurs near the separation point. Then a plateau typical of separated flows can be observed. Finally, a more progressive pressure rise takes place during reattachment.

The root mean square of the wall pressure fluctuations, shown in Fig. 9(c), is amplified near the reflected shock foot. Moreover, wall cooling increases the root-mean-square wall pressure p_{rms}. The heated case produces the lowest p_{rms} among the studied situations. So, even if surface cooling reduces the flow separation, the dynamic loads can be significantly increased.

Figure 9(d) displays the wall heat flux q_w normalized by the constant factor $(\rho_\infty u_\infty C_p T_r)$, allowing a direct comparison between the studied cases. The direction and amount of wall heat flux is better described in this figure rather than the Stanton distribution. Note that because of the imposed wall temperature, the adiabatic condition is not perfectly satisfied in the recirculation region. Still, the heat exchange remains insignificant.

Figure 10 shows contours of the instantaneous skin friction and normalized heat flux for heated SBLI-1.9-9.5 and cooled SBLI-0.5-9.5 wall conditions. We note that regions of reverse flow appears sooner in the heated case. The heat transfer is clearly amplified after the flow separation. The fact that the cooled case has a much smaller viscous length scale is evident in this figure, with clearly smaller flow structures than in the heated case.

E. Pressure spectra

The computation of temporal spectra requires long simulation times, which becomes particularly expensive under cooled wall conditions due to the increased resolution requirements. The premultiplied wall pressure and heat flux spectra $f\,E(f)$ are displayed in Fig. 11 as a function of the Strouhal number $\text{Sr} = f\delta_0/u_\infty$ and the scaled coordinate x^*. The spectra are normalized by the local value of the the root-mean-square quantity, in such a way that their integral over frequency is unity at each streamwise station. The premultiplied power spectral density (PSD) are obtained using Welch's method by splitting the signal in three segments with 50% overlap, which are individually Fourier-transformed. Then, the frequency spectra are obtained by averaging the periodograms of the various segments, minimizing the variance of the PSD estimator. Finally, the PSD is filtered by applying a Konno-Ohmachi smoothing [41] ensuring a constant bandwidth on a logarithmic scale.

The map of the wall pressure signal shows the typical features of this type of flow [22,30]. Upstream of the interaction zone the broadband energy in the premultiplied spectra is typical of a canonical wall-bounded flow, with a peak at $\text{Sr} \approx 1$, associated with the energetic turbulent structures of the boundary layer. Downstream of the interaction, the spectral density is broadened, and the peak

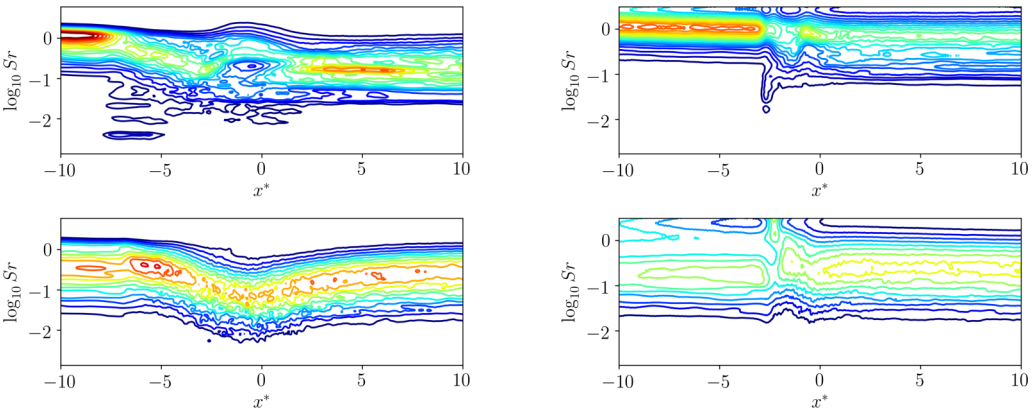

FIG. 11. Contours of premultiplied pressure spectra (top) and heat flux spectra (bottom) $fE(f)$ for flow case assuming heated SBLI-1.9-9.5 (left) and cooled wall SBLI-0.5-9.5 (right). The spectra are normalized in such a way that their integral over frequency is unity, at each streamwise station.

is shifted to lower frequencies due to the thickening of the boundary layer. Note that a limited part of the broadband energy in the premultiplied spectra is found close to the foot of the reflected shock at frequencies two to three orders of magnitude lower than the turbulent structures of the incoming boundary layer. For the heated case, Sr ≈ 0.005, while for the cooled case, Sr ≈ 0.05.

When analyzing the premultiplied heat flux spectra, there is no evidence of low-frequency dynamics and most of the energy is contained at intermediate to high frequencies. However, the heat flux spectra display quite different behaviors between the heated and cooled cases because the former is a strong interaction while the latter is a weak interaction, as already shown. For the heated case, a strong amplification of the heat transfer fluctuations is observed close to the separation and reattachment points, with a shift toward intermediate frequencies, associated with the separated shear layer [20]. For the cooled case, this is not observed.

F. Similarity of the length of the interaction

The extent of the separation region L_{sep} is plotted in Fig. 12(a) as a function of the deflection angle φ. If the angle of the shock generator is kept constant, the separation length is maximum (minimum), when wall heating (cooling) is employed. Similar conclusions are found for the interaction length

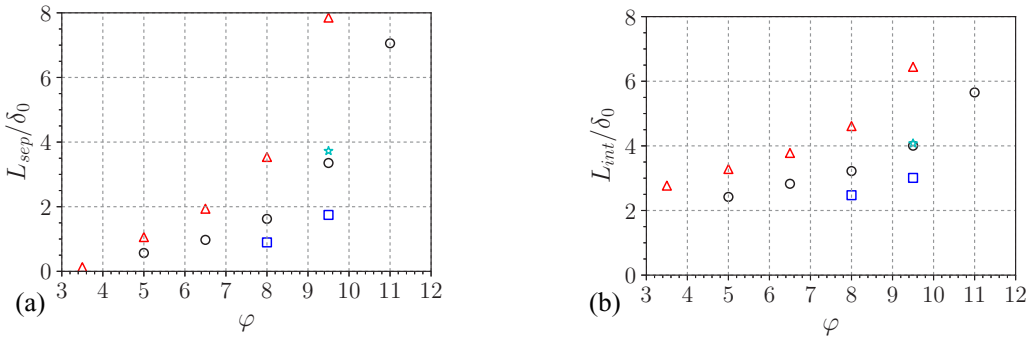

FIG. 12. (a) Separation and (b) interaction length as a function of the deflection angle. (△) heated, (◯) adiabatic, and (□) cooled wall. (⋆) refers to the the adiabatic wall simulation at moderate Reynolds number.

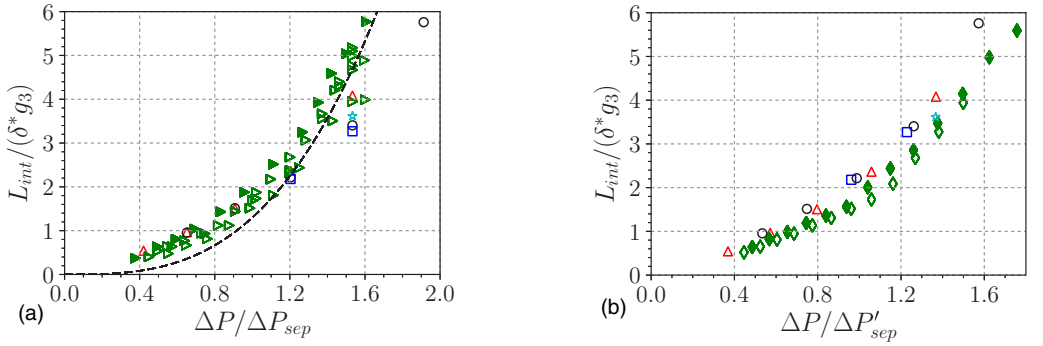

FIG. 13. Normalized interaction length as a function of separation criterions. (△) heated, (◯) adiabatic, and (□) cooled wall. (⋆) refers to the the adiabatic wall simulation at moderate Reynolds number. Compilation of results discussed in Ref. [42] is also reported: (▸) heated walls [43] and (▷) adiabatic walls [9,11,12,44]. Experimental data from IUSTI in Marseille at Mach ($M_\infty = 2.3$) and Reynolds ($\mathrm{Re}_\theta = 5 \times 10^3$) numbers are also reported. (◊) adiabatic walls [29] and (♦) heated walls [29].

L_{int}, shown in Fig. 12(b). Interestingly, for the heated case with $\varphi = 9.5°$, the separation length is larger than the interaction length.

Using mass conservation properties along the interaction, Souverein *et al.* [42] carried out a scaling analysis, where the length of the interaction is normalized by the displacement thickness of the upstream boundary layer δ^* and a function g_3 that takes into account the imposed flow deflection and the Mach number. From their scaling approach, the dimensionless length of interaction is given by

$$L^{\diamond}_{\mathrm{int}} = \frac{L}{\delta^* g_3(\beta,\varphi)} \quad , \quad \text{with} \;\; g_3(\beta,\varphi) = \frac{\sin(\beta-\varphi)}{\sin(\beta)\sin(\varphi)}, \tag{7}$$

where φ and β stand for the deflection and shock angle respectively.

Souverein *et al.* then combined the normalized length of interaction $L^{\diamond}_{\mathrm{int}}$ with a separation criterion S_e and showed that the compilation data obtained from several SBLI studies, spanning different Reynolds and Mach numbers, follows a general trend with limited scatter. They defined the separation criterion as $S_e = \Delta P/\Delta P_{\mathrm{sep}}$, in which ΔP is the shock strength and ΔP_{sep} is the shock intensity needed to make the boundary layer separate. The separation pressure ΔP_{sep} was estimated based on the inviscid properties of the upstream boundary layer as $\Delta P_{\mathrm{sep}} \approx (1/k_1) q_\infty$, where $q_\infty = (1/2)\rho_\infty u_\infty^2$ is the dynamic pressure and k_1 is a constant that slightly depends on the Reynolds number. Quantities ρ_∞ and u_∞ are the density and velocity at the free stream, respectively. For large Reynolds numbers ($1 \times 10^4 < \mathrm{Re}_\theta < 3 \times 10^5$), $k_1 = 2.5$, while for low Reynolds numbers ($\mathrm{Re}_\theta \approx 5 \times 10^3$), a value of $k_1 = 3$ was derived. They showed that this constant was independent on the Mach number. In the present analysis, this parameter is set to $k_1 = 3$ and the displacement thickness of the upstream boundary layer δ^* is computed at $20\delta_{\mathrm{in}}$ (or about $12\delta_0$ upstream of the impingement location x_{imp}).

This criterion was validated on a large number of SBLI (most of them using adiabatic walls) by Souverein *et al.* [42] and it has been recently shown to be valid also for transitional interactions [45]. Surprisingly, results incorporating the effect of heated walls [43] also showed good agreement with the proposed model. As we are dealing with a constant Mach number flow, the deflection angle is a valid representation of the separation criterion S_e [29]. The normalized interaction length is plotted against the separation criterion S_e in Fig. 13(a) together with compilation of data found in the literature. It is clear that most of the heating effects on the interaction length are taken into account by the scaling (7). However, Jaunet *et al.* [29] stated that in order to capture correctly the influence of the heating effects, the computation of ΔP_{sep} should take into account the Mach number M_∞ and the friction

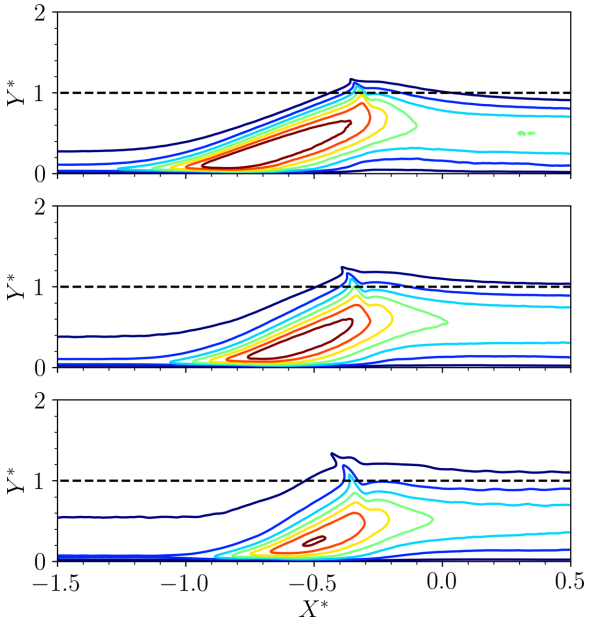

FIG. 14. Mean turbulence kinetic energy $k = \widetilde{u_i'' u_i''}/2$. Cases with $\varphi = 9.5°$: heated (SBLI-1.9-9.5), adiabatic (SBLI-1.0-9.5), and cooled (SBLI-0.5-9.5) wall from top to bottom. Contour levels are shown in the range $0 < k/u_\infty^2 < 0.04$. Coordinates are now scaled as $Y^* = yg_3/L$ and $X^* = (x - x_{\text{imp}})/L$.

coefficient upstream of the boundary layer C_{f0}. Their resulting modified separation criterion S_e' instead uses $\Delta P'_{\text{sep}} = k_2 q_e \sqrt{2C_{f0}/(M_\infty^2 - 1)^{1/2}}$ with $k_2 = 7.14$. The normalized interaction length $L_{\text{int}}^\diamond$ as a function of $\Delta P/\Delta P'_{\text{sep}}$ is plotted in Fig. 13(b) together with the experiments of Jaunet *et al.* for heated and adiabatic walls. The agreement between numerical and experimental results is very good and validates the scaling laws proposed previously [29,42].

Moreover, if the wall-normal coordinate is now scaled as $Y^* = yg_3/L$ and the streamwise coordinate as $X^* = (x - x_{\text{imp}})/L$, as suggested by Souverein *et al.* [42], we note that the vertical extent of the turbulent region developing downstream of the reflecting shock foot is close to unity (Fig. 14). This finding is verified not only for the adiabatic cases but also for the nonadiabatic ones.

G. Influence of a variable wall temperature

The results in the previous section suggest that the change in the interaction length is mainly a consequence of changes in the incoming conditions, in agreement with the findings of Souverein *et al.* [42] and Jaunet *et al.* [29]. This is further investigated here by performing simulations where the wall is taken as adiabatic in the incoming boundary layer and heated in the interaction region, and vice versa. The idea is that these cases with a streamwise varying wall temperature can help separate the effects of the incoming boundary layer and the local conditions in the interaction region. The wall temperature is taken as

$$T_w(x) = T_r \left\{ 1 + \frac{f-1}{2} \left[1 + \tanh \frac{2(x - x_T)}{\delta_{\text{in}}} \right] \right\}, \tag{8}$$

where f is the ratio between the wall temperatures and x_T is the streamwisee coordinate where the transition occurs. This value chosen as the mean location where the interaction starts for the cases with constant wall temperatures, without any attempts at finding the "optimal" values. For the adiabatic-to-heated wall, $f = 1.9$, and for the heated-to-adiabatic wall, $f = 1/1.9$.

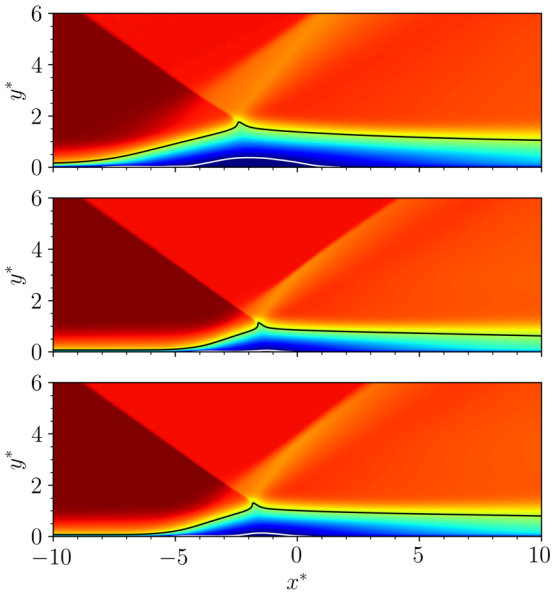

FIG. 15. Mean streamwise velocity field $\overline{u}$. Cases with $\varphi = 9.5^\circ$: heated (SBLI-1.9-9.5), adiabatic (SBLI-1.0-9.5), and variable (adiabatic to heated) wall from top to bottom.

Figure 15 shows that the mean velocity field for the simulation SBLI-adia2heat-9.5 is closer to the simulation with adiabatic walls, at least in terms of interaction length and height scales. A more quantitative analysis is done by plotting the mean friction coefficient distribution for cases with heated, adiabatic, and variable wall temperatures in Fig. 16. The length of the separation zone for the simulation with adiabatic walls in the preinteraction region is closer to the one assuming adiabatic walls everywhere, which supports previous conclusions that the size of the interaction region is linked to the state of the incoming boundary layer. Note that for simulation SBLI-heat2adia-9.5, the boundary layer tries to recover the adiabatic state, but the friction coefficient remains between both

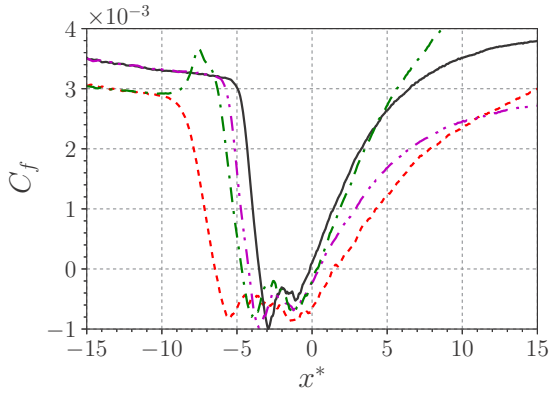

FIG. 16. Distribution of the mean skin friction coefficient across the interaction zone for simulations with adiabatic (SBLI-1.0-9.5, solid), heated (SBLI-1.9-9.5, dashed), variable (SBLI-heat2adia-9.5, dash-dotted line), and variable (SBLI-adia2heat-9.5, dash-double dotted line) wall temperatures.

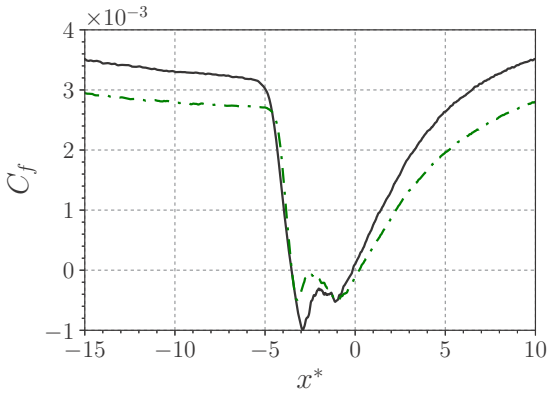

FIG. 17. Distribution of the mean skin friction coefficient across the interaction zone for the adiabatic case at low (solid) and moderate (dash-dotted line) Reynolds number flows.

references. Therefore, if the primary objective is to reduce flow separation, it is clear that one must modify the wall temperature in a sufficiently large region around the shock impingement zone.

H. Influence of the Reynolds number

A simulation assuming adiabatic walls at higher Reynolds number ($\mathrm{Re}_\tau^* = 885$) was also performed to investigate the influence of this parameter on the size of the mean separation bubble. Details about the grid spacing and characteristics of the boundary layer at the station where the shock impinges are found in Tables I and II. For the boundary layer simulation, a good agreement was found with recently published data [36] in terms of statistical quantities. Results are omitted for brevity.

For the SBLI case, the size of the interaction length does not appear to be significantly affected by the Reynolds number (at least for the ones considered here), in agreement with the findings of Morgan *et al.* [46]. Figure 17 plots the skin friction across the interaction for simulation at low ($\mathrm{Re}_\theta \approx 1000$) and moderate ($\mathrm{Re}_\theta \approx 2000$) Reynolds numbers. As expected, we see that increasing the Reynolds number decreases the friction coefficient of the incoming boundary layer. Second, the magnitude of the first negative skin friction peak decreases. Moreover, as the Reynolds number is increased, it is possible to obtain a region where two distinct separation bubbles coexist. We also notice that the size of the interaction does not appear to be significantly affected by Reynolds number (see also Fig. 12). Therefore, over the limited range considered, it appears that the impact of the shock strength or wall cooling is more important than the Reynolds number in determining the size of the interaction length scales.

Interestingly, the difference in the Reynolds number explains the discrepancy observed between numerical results and experimental data in Fig. 13. Even if changing the Reynolds number does not affect significantly the size of the interaction L_{int}, it does affect the incoming boundary layer and thus the scaling quantities. As a consequence, the DNS results move toward the experimental points at higher Reynolds numbers.

This analysis confirms that the reduced Reynolds number database generated in the present work is suitable to study and measure the influence of wall cooling on the SBLI flow field.

I. Weak vs strong interactions

Defining whether a SBLI flow is separated or not can be ambiguous, especially when comparing experimental and numerical results. Practically all simulations performed in this study show a recirculation region (with the exception of SBLI-1.9-3.5). However, it is straightforward to classify

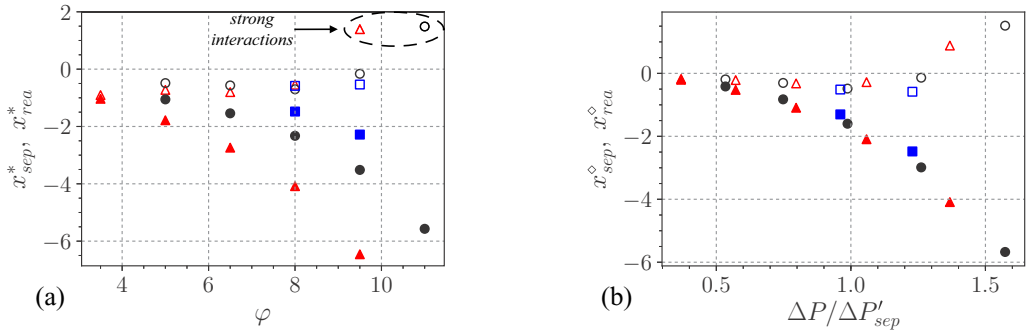

FIG. 18. Normalized separation and reattachment positions normalized by δ_0 vs deflection angle (a) and normalized by δ_0/g_3 vs separation criterion (b). (△) heated, (◯) adiabatic, and (□) cooled wall. Full symbols refer to the separation point and empty symbols to the reattachment point.

them by the strength of the interaction. One way to distinguish them is by the two bumps in the wall pressure distribution [Fig. 7(b)]. Another way is by analyzing the heat release or the Stanton number distribution [Fig. 7(c)]. A third way is through the separation and reattachment location of the mean bubble [Fig. 18(a)]. It is interesting to note that for separated cases with weak interactions, the flow conditions (shock strength and wall condition) have a larger impact on the separation position x^*_{sep} than the reattachment point x^*_{rea}; i.e., the reattachment location remains practically unchanged for weak interactions. This may explain why all curves cross the same point ($x^* \approx -1$), before gradually relaxing toward the inviscid value (Fig. 19). When the interaction is strong, both locations are affected (see cases SBLI-1.9-9.5 and SBLI-1.0-11.0). Therefore, as explained in Ref. [3], there is first a pressure rise at the separation location, followed by a pressure plateau inside the bubble and a second pressure rise at the reattachment.

The normalization (7) is applied to the separation and reattachment positions and plotted as a function of the modified separation criterion in Fig. 18(b). One notes that two distinct linear regions are present for both separation and reattachment locations, in accordance with the analysis carried out for the interaction region. While the reattachment point practically does not move until $\Delta P/\Delta P'_{\text{sep}} \approx 1.2$, for larger values of pressures ratios there is notably a jump that makes the x^*_{rea} move downstream.

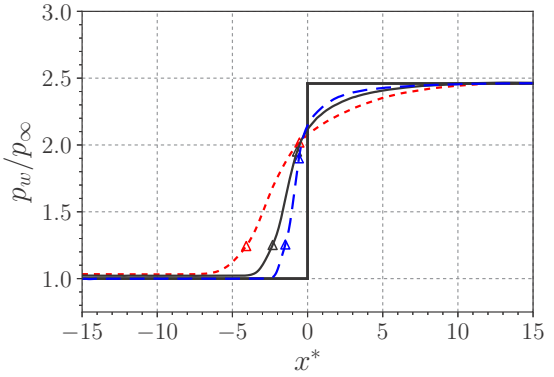

FIG. 19. Distribution of the mean wall pressure across the interaction zone at various wall-to-recovery-temperature ratios and deflection angle 8.0°: cases SBLI-1.9-8.0 (dotted), SBLI-1.0-8.0 (solid), and SBLI-0.5-8.0 (dashed lines). Separation and reattachment locations are also shown with symbols.

V. SUMMARY

The influence of the wall thermal condition on the canonical case of an impinging shock wave interacting with a turbulent supersonic boundary layer is a research topic that is underexplored. In the present work, adiabatic ($T_w/T_r = 1.0$), heated ($T_w/T_r = 1.9$), and cooled ($T_w/T_r = 0.5$) wall conditions are considered for the SBLI at free-stream Mach number $M_\infty = 2.28$ and several shock angles. It is observed that wall heating increases the interaction scales and size of the separation bubbles. On the contrary, wall cooling minimizes the flow separation but has the drawback of increasing the wall pressure fluctuations, which could have an impact on structural integrity of high-speed vehicles. The distribution of the Stanton number shows a good agreement with prior experimental studies and confirms the strong heat transfer and complex pattern within the interaction region. Numerical results indicate that the changes in the interaction length are mainly linked to the incoming boundary layer through the displacement thickness δ^* and friction coefficient C_{f0}, as suggested in previous studies [29,42]. The same normalization used for the scaling analysis were applied to investigate the separation and reattachment positions. The reattachment location was less impacted by the flow conditions, remaining practically unchanged for weak interactions. Simulations performed with variable wall temperature confirmed the scaling analysis, and we conclude that if the objective is to reduce the flow separation, cooling must be applied in a sufficiently large region to modify the incoming boundary layer; it is not sufficient to merely modify the conditions exactly at the interaction.

ACKNOWLEDGMENTS

P.V. and J.L. were supported by the Air Force Office of Scientific Research (Grant No. FA9550-16-1-0385). M.B. was supported by the Scientific Independence of Young Researchers Program 2014 (Active Control of Shock-Wave Boundary-Layer Interaction Project, Grant No. RBSI14TKWU), funded by MIUR. The work was performed using HPC resources at the University of Maryland (DeepThought2) and the Maryland Advanced Research Computing Center (MARCC).

[1] D. S. Dolling, Fifty years of shock-wave/boundary-layer interaction research: What next? AIAA J. **39**, 1517 (2001).

[2] A. J. Smits and Jean-Paul Dussauge, *Turbulent Shear Layers in Supersonic Flow* (Springer Science & Business Media, Berlin, 2006).

[3] J. Délery and J.-P. Dussauge, Some physical aspects of shock wave/boundary layer interactions, Shock Waves **19**, 453 (2009).

[4] H. Babinsky and J. K. Harvey, *Shock Wave-Boundary-Layer Interactions* (Cambridge University Press, Cambridge, UK, 2011), Vol. 32.

[5] N. T. Clemens and V. Narayanaswamy, Low-frequency unsteadiness of shock wave/turbulent boundary layer interactions, Annu. Rev. Fluid Mech. **46**, 469 (2014).

[6] J. Délery and J. G. Marvin, Shock-wave boundary layer interactions, Tech. Rep. AGARDograph 280. AGARD, Neuilly Sur Seine, France (1986).

[7] G. S. Settles and D. S. Dolling, Swept shock/boundary-layer interactions - Tutorial and update, AIAA Paper No. 90-0375 (1990).

[8] F. O. Thomas, C. M. Putnam, and H. C. Chu, On the mechanism of unsteady shock oscillation in shock wave/turbulent boundary layer interactions, Exp. Fluids **18**, 69 (1994).

[9] P. Dupont, C. Haddad, and J. F. Debieve, Space and time organization in a shock-induced separated boundary layer, J. Fluid Mech. **559**, 255 (2006).

[10] J.-P. Dussauge, P. Dupont, and J.-F. Debiève, Unsteadiness in shock wave boundary layer interactions with separation, Aerosp. Sci. Technol. **10**, 85 (2006).

[11] S. Piponniau, J. P. Dussauge, J. F. Debieve, and P. Dupont, A simple model for low-frequency unsteadiness in shock-induced separation, J. Fluid Mech. **629**, 87 (2009).
[12] L. J. Souverein, P. Dupont, J.-F. Debiève, B. W. Van Oudheusden, and F. Scarano, Effect of interaction strength on unsteadiness in shock-wave-induced separations, AIAA J. **48**, 1480 (2010).
[13] N. A. Adams, Direct simulation of the turbulent boundary layer along a compression ramp at $M = 3$ and Re $[\theta] = 1685$, J. Fluid Mech. **420**, 47 (2000).
[14] D. P. Rizzetta, M. R. Visbal, and D. V. Gaitonde, Large-eddy simulation of supersonic compression-ramp flow by high-order method, AIAA J. **39**, 2283 (2001).
[15] M. Wu and M. P. Martin, Analysis of shock motion in shockwave and turbulent boundary layer interaction using direct numerical simulation data, J. Fluid Mech. **594**, 71 (2008).
[16] S. Priebe, M. Wu, and M. P. Martin, Direct numerical simulation of a reflected-shock-wave/turbulent-boundary-layer interaction, AIAA J. **47**, 1173 (2009).
[17] E. Touber and N. D. Sandham, Large-eddy simulation of low-frequency unsteadiness in a turbulent shock-induced separation bubble, Theor. Comput. Fluid Dyn. **23**, 79 (2009).
[18] S. Pirozzoli and M. Bernardini, Direct numerical simulation database for impinging shock wave/turbulent boundary-layer interaction, AIAA J. **49**, 1307 (2011).
[19] A. Hadjadj, Large-eddy simulation of shock/boundary-layer interaction, AIAA J. **50**, 2919 (2012).
[20] G. Aubard, X. Gloerfelt, and J.-C. Robinet, Large-eddy simulation of broadband unsteadiness in a shock/boundary-layer interaction, AIAA J. **51**, 2395 (2013).
[21] J. Matheis and S. Hickel, On the transition between regular and irregular shock patterns of shock-wave/boundary-layer interactions, J. Fluid Mech. **776**, 200 (2015).
[22] J. W. Nichols, J. Larsson, M. Bernardini, and S. Pirozzoli, Stability and modal analysis of shock/boundary layer interactions, Theor. Comput. Fluid Dyn. **31**, 33 (2017).
[23] V. Pasquariello, S. Hickel, and N. A. Adams, Unsteady effects of strong shock-wave/boundary-layer interaction at high Reynolds number, J. Fluid Mech. **823**, 617 (2017).
[24] F. W. Spaid and J. C. Frishett, Incipient separation of a supersonic, turbulent boundary layer, including effects of heat transfer, AIAA J. **10**, 915 (1972).
[25] L. H. Back and R. F. Cuffel, Shock wave/turbulent boundary-layer interactions with and without surface cooling, AIAA J. **14**, 526 (1976).
[26] M. Hayashi, A. Sakurai, and S. Aso, Measurement of heat-transfer coefficients in shock wave-turbulent boundary layer interaction regions with a multi-layered thin film heat transfer gauge, NASA Tech. Memo. TM-77958 (1986), p. 455.
[27] E. Schülein, Skin friction and heat flux measurements in shock/boundary layer interaction flows, AIAA J. **44**, 1732 (2006).
[28] N. D. Sandham, E. Schülein, A. Wagner, S. Willems, and J. Steelant, Transitional shock-wave/boundary-layer interactions in hypersonic flow, J. Fluid Mech. **752**, 349 (2014).
[29] V. Jaunet, J. F. Debiève, and P. Dupont, Length scales and time scales of a heated shock-wave/boundary-layer interaction, AIAA J. **52**, 2524 (2014).
[30] M. Bernardini, I. Asproulias, J. Larsson, S. Pirozzoli, and F. Grasso, Heat transfer and wall temperature effects in shock wave turbulent boundary layer interactions, Phys. Rev. Fluids **1**, 084403 (2016).
[31] F. Ducros, F. Laporte, T. Souleres, V. Guinot, P. Moinat, and B. Caruelle, High-order fluxes for conservative skew-symmetric-like schemes in structured meshes: application to compressible flows, J. Comput. Phys. **161**, 114 (2000).
[32] E. Johnsen, J. Larsson, A. V. Bhagatwala, W. H. Cabot, P. Moin, B. J. Olson, P. S. Rawat, S. K Shankar, B. Sjögreen, H. C. Yee *et al.*, Assessment of high-resolution methods for numerical simulations of compressible turbulence with shock waves, J. Comput. Phys. **229**, 1213 (2010).
[33] M. Klein, A. Sadiki, and J. Janicka, A digital filter based generation of inflow data for spatially developing direct numerical or large eddy simulations, J. Comput. Phys. **186**, 652 (2003).
[34] H.-H. Fernholz and P. J. Finley, A critical compilation of compressible turbulent boundary layer data, Tech. Rep. AGARDograph 223. AGARD, Neuilly sur Seine, France (1997).
[35] A. Trettel and J. Larsson, Mean velocity scaling for compressible wall turbulence with heat transfer, Phys. Fluids **28**, 026102 (2016).

[36] P. Schlatter and R. Örlü, Assessment of direct numerical simulation data of turbulent boundary layers, J. Fluid Mech. **659**, 116 (2010).
[37] D. Modesti and S. Pirozzoli, Reynolds and Mach number effects in compressible turbulent channel flow, Int. J. Heat Fluid Flow **59**, 33 (2016).
[38] A. Walz, *Compressible Turbulent Boundary Layers* (CNRS, 1962), pp. 299–350.
[39] Y.-S. Zhang, W.-T. Bi, F. Hussain, and Z.-S. She, A generalized Reynolds analogy for compressible wall-bounded turbulent flows, J. Fluid Mech. **739**, 392 (2014).
[40] H. Babinsky, Y. Li, and C. W. Pitt Ford, Microramp control of supersonic oblique shock-wave/boundary-layer interactions, AIAA J. **47**, 668 (2009).
[41] K. Konno and T. Ohmachi, Ground-motion characteristics estimated from spectral ratio between horizontal and vertical components of microtremor, Bull. Seismol. Soc. Am. **88**, 228 (1998).
[42] L. J. Souverein, P. G. Bakker, and P. Dupont, A scaling analysis for turbulent shock-wave/boundary-layer interactions, J. Fluid Mech. **714**, 505 (2013).
[43] H. Laurent, Turbulence d'une interaction onde de choc/couche limite sur une paroi plane adiabatique ou chauffée, Ph.D. thesis, Université d'Aix-Marseille II, 1996.
[44] L. J. Souverein, B. W. Van Oudheusden, F. Scarano, and P. Dupont, Application of a dual-plane particle image velocimetry (dual-PIV) technique for the unsteadiness characterization of a shock wave turbulent boundary layer interaction, Meas. Sci. Technol. **20**, 074003 (2009).
[45] R. Quadros and M. Bernardini, Numerical investigation of transitional shock-wave/boundary-layer interaction in supersonic regime, AIAA J. **56**, 2712 (2018).
[46] B. Morgan, S. Kawai, and S. K. Lele, A parametric investigation of oblique shockwave/turbulent boundary layer interaction using LES, AIAA Paper No. 2011-3430 (2011).